Available online at www.sciencedirect.com

ScienceDirect

Acta Materialia 83 (2015) 37–47

Acta MATERIALIA

www.elsevier.com/locate/actamat

Grain boundary segregation in Fe–Mn–C twinning-induced plasticity steels studied by correlative electron backscatter diffraction and atom probe tomography

M. Herbig,[a,*] M. Kuzmina,[a] C. Haase,[b] R.K.W. Marceau,[a,c] I. Gutierrez-Urrutia,[a,d] D. Haley,[a,e] D.A. Molodov,[b] P. Choi[a] and D. Raabe[a]

[a] *Max-Planck-Institut für Eisenforschung, Department of Microstructure Physics and Alloy Design, 40237 Düsseldorf, Germany*
[b] *Institut für Metallkunde und Metallphysik, Rhein-Westfälische Technische Hochschule Aachen, Kopernikusstraße 14, 52056 Aachen, Germany*
[c] *Deakin University, Institute for Frontier Materials, Geelong Waurn Ponds Campus, VIC 3216, Australia*
[d] *Research Center for Strategic Materials/National Institute for Materials Science, 1-2-1 Sengen, Tsukuba-city, Ibaraki 305-0047, Japan*
[e] *University of Oxford, Department of Materials, Parks Road, Oxford OX1 3PH, UK*

Received 22 August 2014; revised 15 September 2014; accepted 21 September 2014

Abstract—We report on the characterization of grain boundary (GB) segregation in an Fe–28Mn–0.3C (wt.%) twinning-induced plasticity (TWIP) steel. After recrystallization of this steel for 24 h at 700 °C, ~50% general grain boundaries (GBs) and ~35% Σ3 annealing twin boundaries were observed (others were high-order Σ and low-angle GBs). The segregation of B, C and P and traces of Si and Cu were detected at the general GB by atom probe tomography (APT) and quantified using ladder diagrams. In the case of the Σ3 coherent annealing twin, it was necessary to first locate the position of the boundary by density analysis of the atom probe data, then small amounts of B, Si and P segregation and, surprisingly, depletion of C were detected. The concentration of Mn was constant across the interface for both boundary types. The depletion of C at the annealing twin is explained by a local change in the stacking sequence at the boundary, creating a local hexagonal close-packed structure with low C solubility. This finding raises the question of whether segregation/depletion also occurs at Σ3 deformation twin boundaries in high-Mn TWIP steels. Consequently, a previously published APT dataset of the Fe–22Mn–0.6C alloy system, containing a high density of deformation twins due to 30% tensile deformation at room temperature, was reinvestigated using the same analysis routine as for the annealing twin. Although crystallographically identical to the annealing twin, no evidence of segregation or depletion was found at the deformation twins, owing to the lack of mobility of solutes during twin formation at room temperature.

Keywords: Twin grain boundary; Austenite; Atom probe tomography; Electron backscatter diffraction; Grain boundary segregation

1. Introduction

Fe–Mn–C twinning-induced plasticity (TWIP) steels represent a novel grade of advanced high-strength and formable austenitic steels with high potential for automotive and related sheet-forming applications [1–12]. Knowledge of equilibrium grain boundary (GB) segregation in these austenitic steels is required to better understand the local concentration dependence of associated phenomena, e.g. the mobility of GBs, and thereby the kinetics of grain growth or recrystallization during thermomechanical treatment [13,14]. Furthermore, GB segregation can affect the twinning behavior of TWIP steels since the critical stress for deformation twin formation is directly related to the stacking fault energy (SFE) [3,15,16], which is a function of the chemical composition [17,18]. Therefore, a change in the local chemical composition at GBs should influence the critical stress necessary for the onset of twin nucleation at GBs and hence the strain hardening behavior.

In addition to the influence of GB segregation on twinning, better understanding is required of its effect on failure phenomena in TWIP steels. Room temperature fracture behavior of TWIP steels is normally ductile, with cup–cone dimples on the fracture surface [2,19], though there are reports that higher Mn contents slightly increase the fraction of intergranular cracking [20,21], which mainly nucleates at MnS inclusions [22]. Stress corrosion cracking is another relevant fracture mechanism [23], as is the corrosion behavior in general, since segregation causes local differences in the chemical potential [24]. A related aspect that

* Corresponding author. Tel.: +49 211 6792 538; fax: +49 211 6792 333; e-mail: m.herbig@mpie.de

http://dx.doi.org/10.1016/j.actamat.2014.09.041
1359-6462/

is attracting great interest is the hydrogen embrittlement of high-Mn steels [25–29]. Hydrogen has been also shown to deteriorate mechanical properties in general, leading to intergranular fracture [30–32]. Hydrogen-induced delayed fracture of TWIP steels has been reported for cup-drawn specimens in air [25] and hydrogen-assisted cracking has been observed to affect all boundary types, surprisingly including Σ3 coherent annealing twins and deformation twins [29]. He et al. [33] investigated the segregation of hydrogen to Σ3 (1 1 1) boundaries in α-iron by first-principles calculations and concluded that the segregation of Cr reduces the segregation of hydrogen. This result indicates that the presence of other segregated elements at boundaries can potentially reduce the impact of hydrogen embrittlement. It is thus a motivation for the investigation of GB equilibrium segregation [34,35] in TWIP steels.

Knowledge of the local grain boundary chemistry is needed to understand the above-mentioned phenomena. Atom probe tomography (APT), with its near-atomic spatial resolution and high detection sensitivity (in the range of a few parts per million, and equal for all elements), is a powerful tool for the characterization of segregation phenomena at buried interfaces that occur within a few angstroms around the boundary plane and often involve light elements [36–41]. In the current work, segregation was evaluated by quantitative APT analyses of three boundary types: a general GB (also called a random GB), referring to a high-angle grain boundary (HAGB) the configuration of which does not correspond to a special boundary type according to coincident site lattice (CSL) theory; an annealing twin, created by diffusion during an extended heat treatment; and a deformation twin, created by mechanical deformation at room temperature [42,43]. The first two were identified by electron backscattering diffraction (EBSD), the deformation twins by transmission electron microscopy. All boundaries were prepared by site-specific focused ion beam (FIB) lift-out techniques [44].

2. Experimental

A high-Mn TWIP steel with nominal composition Fe–28Mn–0.3C (wt.%) was cast into 140 × 140 mm ingots, followed by hot rolling in three passes at 1150 °C to 50 mm thickness, homogenization for 5 h at 1200 °C, hot rolling in 12–14 passes to 3 mm, cold rolling to 2 mm and air cooling. The sample was recrystallized by annealing for 24 h at 700 °C followed by water quenching, then ground to the middle layer of the sheet. All heat treatments were performed in an air circulation furnace. The long annealing time was applied to generate a microstructure coarse enough to efficiently perform site-specific lift-out preparation of selected boundaries using the FIB. The chemical compositions according to wet-chemical and atom probe analyses are given in Table 1.

Metallographic preparation for scanning electron microscopy (SEM) was performed along the rolling direction–transverse direction (RD–TD) plane. The sample was ground successively using SiC grinding paper, followed by polishing with 3 and 1 μm diamond suspensions. Electropolishing was subsequently performed at room temperature for 20 s using a Struers LectroPol-5, with a flow rate of 10, at 22 V using an electrolyte consisting of 83 vol.% ethanol, 11 vol.% butyl glycol and 6 vol.% perchloric acid. EBSD mapping and the site-specific preparation of atom probe samples were performed in a FEI Helios NanoLab 600i dual-beam FIB/SEM instrument. EBSD was performed using a 0.25 μm step size, a 14 mm working distance, a 30 kV acceleration voltage, a 2.7 nA current and a detector system by EDAX. EBSD data analysis was performed with the OIM Data Analysis 7.0.1. (EDAX Inc.) software. Statistical analysis of grain size and GB type were carried out considering all GBs above 2° misorientation angle on an area of 25×10^3 μm^2, containing ~600 complete grains. The average grain diameter was 5.4 μm. We applied the Brandon criterion [45] $15°/\sqrt{\Sigma}$ to identify special GBs with misorientations in the vicinity of low Σ CSL orientation [46]. The sample measured in the current work contained 4% low-angle grain boundaries (LAGBs) with misorientation angles below 15°, 36% Σ3 GBs, 11% other Σ-type GBs and 49% general GBs (Fig. 1). Among the Σ3 GBs, 89% had a grain boundary surface trace that was within 5° deviation from a {1 1 1} plane of each of the abutting grains and were therefore considered to be coherent twin boundaries [47]. As more than 80% of all GBs in this alloy were classified as either general GBs or Σ3 coherent twin boundaries, the characterization of these two types of boundaries can be considered as representative with respect to GB segregation in this material.

The APT samples containing a general GB (52.11° misorientation about the [0.55 0.69 0.47] axis, GB1) and a Σ3 coherent annealing twin (59.83° misorientation about the [0.58 0.58 0.58] axis, GB2) (Fig. 1) were prepared using a site-specific FIB lift-out procedure [44]. The locations of the grain boundaries were carefully tracked and centered throughout all steps of preparation, as illustrated in Figs. 2 and 3. Final milling was performed at 5 kV. APT characterization was conducted on a LEAP 3000X HR instrument (Cameca) operating in voltage mode with a set-point temperature of 60 K, a 15–20% pulse fraction, a 200 kHz pulse repetition rate and a detection rate of 0.005–0.01 atoms per pulse. The total voltage during probing was in the range of 4–9 kV. The peak assignment of carbon was performed as described by Marceau et al. [48]. Tomographic reconstruction was carried out using the IVAS 3.6.6 software. The Gibbs interfacial excess values (in atoms nm^{-2}) for all elements were determined from ladder diagram plots [49,50], which are cumulative plots of a specific atomic species against the cumulative number of all atoms along a region of interest (ROI) positioned perpendicular across the GB in the 3-D atom maps.

3. Results

Fig. 4 illustrates the crystallographic analysis of the plane orientation of GB2. The analysis of the surface trace of GB2 in the EBSD dataset shows that the GB plane is parallel to the surface trace of a {1 1 1} plane in each of the abutting grains (Fig. 4a). As measured on the SEM micrograph of the lift-out sample, the GB plane inclination angle in depth is 16° (Fig. 4b). Fig. 4c shows the standard stereographic projection of the ⟨1 1 1⟩ poles of both grains illustrated using the TOCA software [51,52]. The surface trace of the GB plane is marked as a black line. The GB plane normal must fulfill two criteria: on the one hand, it must be perpendicular to the surface trace (must be situated on the dashed black line), and on the other hand, it must be inclined by 16° with respect to the sample surface plane, as

Table 1. Wet-chemical, bulk composition analysis and atom probe peak-decomposed chemical analysis of a 20 × 40 × 70 nm^3 region without a GB.

Element	Fe	C	Mn	Si	P	S	Cr	Ni	
Wet-chemical (wt.%)	Balance	0.282	28	0.103	0.0084	<0.0005	0.016	0.037	
Atom probe (wt.%)	Balance	0.40	28	0.09	0.00	–	–	–	
Element	Mo	Al	Cu	Co	Nb	V	Sn	N	B
Wet-chemical (wt.%)	0.02	0.0054	0.0098	0.011	0.027	0.021	<0.0005	0.016	Not tested
Atom probe (wt.%)	–	–	0.01	–	–	–	–	–	–

Elements that were not detected in the atom probe mass spectrum are marked as "–".

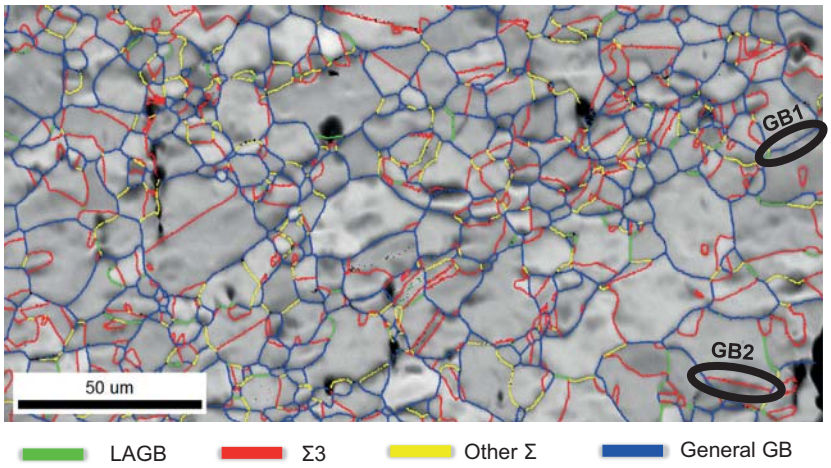

Fig. 1. Overlay of EBSD image-quality map with a color-coded GB network, viewed along the normal direction. Low-angle grain boundaries between 2 and 15° misorientation angle are labeled in green; Σ3 GBs (annealing twins) are in red; other Σ-type GBs are in yellow; and all other HAGBs (general GBs) are in blue. GB1 and GB2 indicate the locations where site-specific FIB lift-outs and subsequent atom probe measurements were performed. (For interpretation of the references to colour in this figure legend, the reader is referred to the web version of this article.)

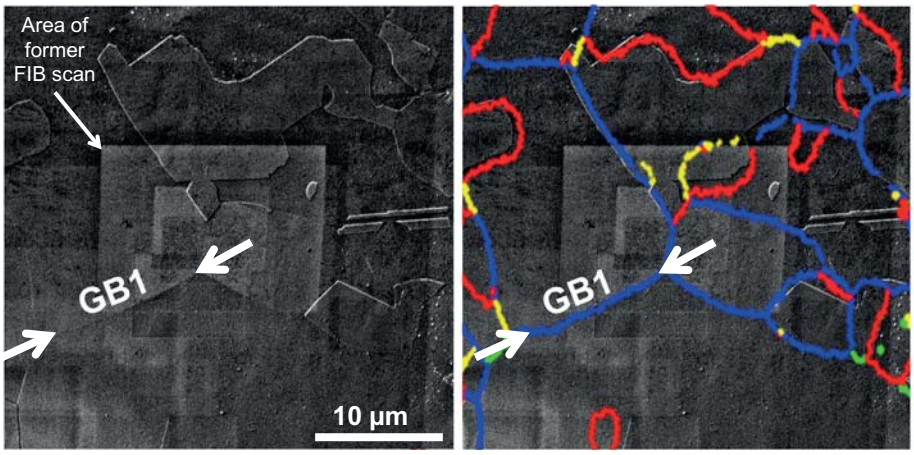

Fig. 2. Identification of the specific grain boundary for site-specific APT sample preparation. (a) SEM image of the region of interest. Most grain boundaries are visible due to topological contrast from the electrochemical sample preparation procedure. The contrast of GB1 was further enhanced by FIB etching. (b) Overlay of (a) with the grain boundary network extracted from EBSD mapping (same color coding applied as in Fig. 1).

measured in Fig. 4b. The position marked X (Fig. 4c) fulfills these requirements. At the same location, a ⟨1 1 1⟩ pole of each of the abutting grains coincide. The grain misorientation of GB2 is 60°[1 1 1] and the GB plane is parallel to {1 1 1} with respect to both abutting grains. GB2 is therefore by definition a face-centered cubic (fcc) Σ3 coherent twin boundary. The GB plane of GB1 was not investigated any further as the grain misorientation relationship is sufficient for its identification as a general GB.

3-D atom maps of GB1 and GB2 are shown in Figs. 5 and 6, respectively. In contrast to GB1, in the case of GB2, the concentration changes at the GB were so low that the boundary was neither visible as a point cloud of certain elements nor detectable using conventional visualization tools (iso-concentration surfaces). The position of the GB in the dataset was verified using the color-coded volume renderer tool within the IVAS 3.6.6 software. After smoothing out fine-scale local density variations by

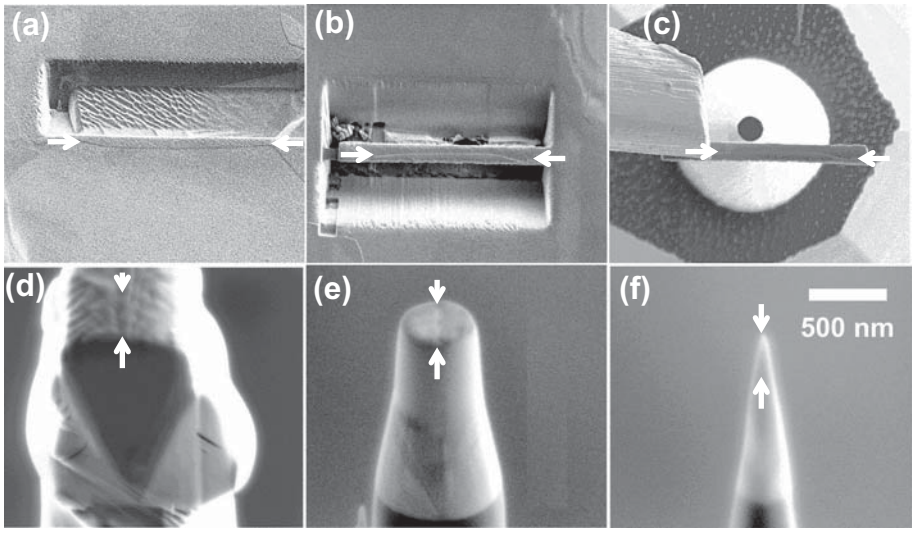

Fig. 3. Site-specific APT sample preparation of GB1 (see also Figs. 1 and 2). White arrows mark the position of the GB. (a) FIB milling of the first trench at the GB. (b) FIB milling of the second trench at the GB and side-cut (sample 180° rotated with respect to (a)). (c) Transport of the triangular prismatic lift-out containing the region of interest to a Si post using a micromanipulator. (d) Attachment of lift-out sample using FIB-assisted Pt deposition (view rotated 90° with respect to (c)). (e) Annular milling of lift-out on Si post. (f) Final shape of the APT sample after low-kV milling.

applying a delocalization of 6 nm in the x, y and z directions and selecting an appropriate color map, the GB position becomes apparent as a planar low-density feature (Fig. 6, bottom right). By positioning an ROI vertically across this low-density region and plotting the elemental concentrations across it as described above, clear evidence for the segregation/depletion of certain elements at the Σ3 coherent annealing twin boundary were obtained and quantified (Fig. 7). The excess values for GB1 and GB2 are summarized in Table 2. The error due to manual peak fitting of the ladder diagrams was estimated using an upper and lower bounds approach. The segregation of B and P is about five times higher in the case of the general GB compared to the Σ3 coherent twin boundary. The amount of Si segregation is higher in the case of the Σ3 coherent twin boundary. Traces of Cu segregation can be only detected in the case of the general GB. The most striking difference between the two GB types is the C content. In the case of the general GB, the C excess is at least a factor of 10 higher than all other excess values, whilst in the case of the Σ3 annealing twin there is a pronounced depletion of C, which is 10 times larger than the strongest segregating solute species, Si (see Table 2).

The bottom right-hand-side image in Fig. 6 provides clear evidence that the APT dataset contains information about the reduced mass density at GB2, so an attempt was made to quantify this density decrease. For this purpose, the numbers of missing Fe and Mn atoms (the matrix and substitutional elements) per interface area were determined from the same ROI that was also employed for the quantification of the excess values at GB2. From the plot of the cumulative number of Fe/Mn atoms over the distance normal to the GB, an average value of about 90 missing Fe/Mn atoms per nm^2 of interface was quantified. A {111} monolayer of fcc iron contains about 18 Fe atoms per nm^2. This means that about five monolayers of {111} fcc iron would be missing at GB2; however, an absence of more than a single monolayer is non-physical. Also, high-resolution transmission electron microscopy (HRTEM) indicates that there are only marginal density differences between Σ3 coherent twins and the matrix [53]. Therefore, the large amounts of missing matrix and substitutional elements that were measured by APT at GB2 are most likely due to atom probe artifacts caused by the different field evaporation behaviors of the two abutting grains. We conclude, as also demonstrated by Felfer et al. [54], that the density at GBs as measured by APT is affected by a combination of inherent field evaporation characteristics of the system (elemental field evaporation potentials in concert with their local arrangement within the crystallographic architecture) that can produce inaccuracies in the measurement that are significantly greater than the signal of interest.

4. Discussion

GB segregation was quantified (Table 2) from ladder diagram plots [49], examples of which are shown in Fig. 7. This approach takes only the integrated number of excess atoms per GB area into account. The shape of the concentration profile across the boundary, including the maximum peak height and the width of the segregation zone, is deliberately ignored as it is subject to well-known atom probe artifacts, such as the local magnification effect or preferential field retention/evaporation effects [55]. As demonstrated for GB2, the statistically robust ladder diagrams are excellent tools with which to quantify small amounts of segregation to planar defects that are neither visible to the human eye in 3-D atom maps nor can be visualized by iso-concentration surfaces.

4.1. Segregation to the general GB (GB1)

In the case of the investigated general grain boundary GB1, the measured segregated elements at the interface are in good agreement with the literature. Lejcek and Hofmann [56] reported that both P and C are attracted by GBs in austenite. Tomozawa et al. [39] reported segregation of P, B and C to general GBs in 316L austenitic stainless steel

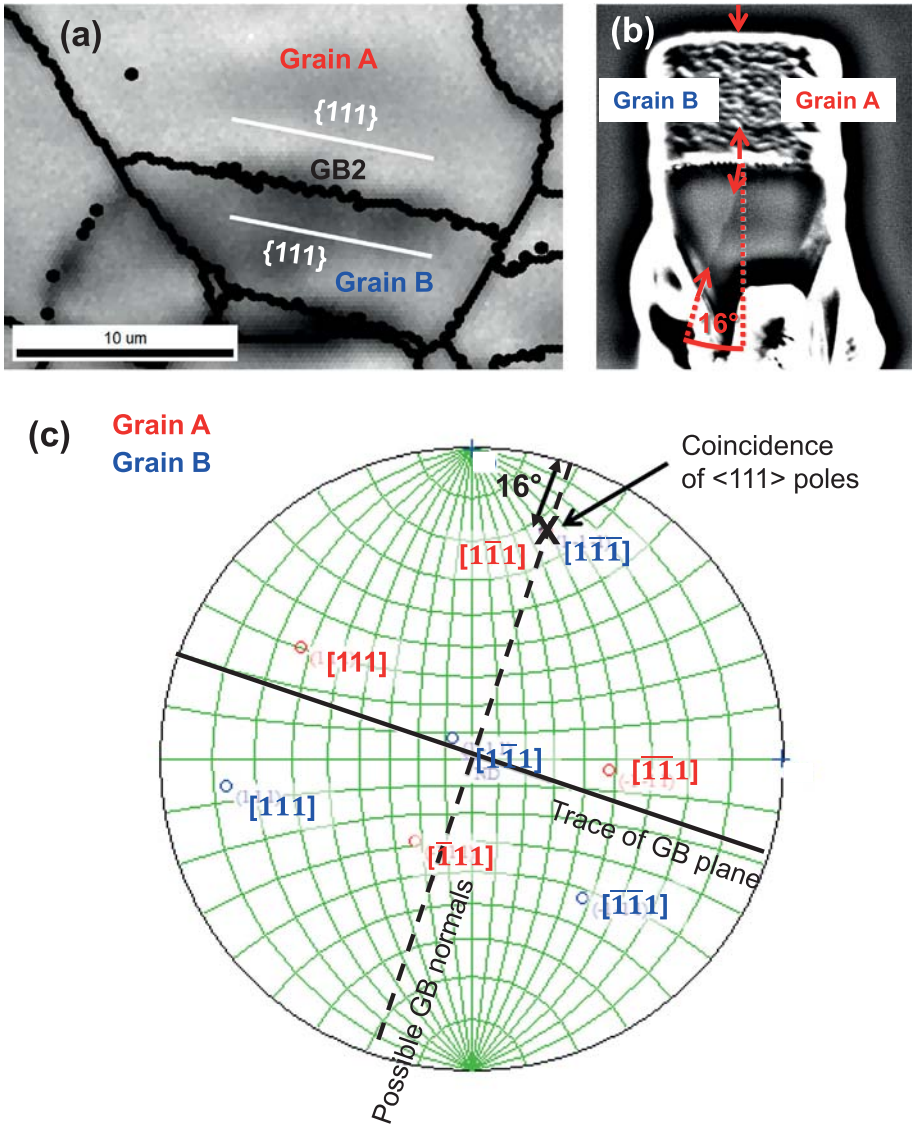

Fig. 4. Determination of the GB plane orientation of GB2. (a) EBSD analysis shows that the surface trace of the GB plane is parallel to the surface trace of a {1 1 1} plane in each of the abutting grains. (b) The SEM image of the lift-out of GB2 after contrast enhancement enables quantification of the GB inclination angle in depth. (c) Standard stereographic projection of the ⟨1 1 1⟩ poles of both grains. The pole of the GB plane is marked by an X. A ⟨1 1 1⟩ pole of each of the abutting grains coincide at the same location. The plane of GB2 can thus be identified as {1 1 1} plane with respect to the crystal lattice of both grains that constitute this boundary.

that was solution-treated at 1043 °C for 15 h and water quenched. In contrast, segregation of S to GBs is known to be greatly reduced in the presence of Mn due to the formation of manganese sulfides [57]. According to Lejcek and Hofmann [56], there is a slight tendency for Si and Mn to become enriched at austenitic GBs. However, Paju and Grabke [58] reported the absence of Mn segregation at GBs in austenite. Whilst GB segregation of Si is confirmed by our measurements, we found no evidence of GB segregation of Mn.

4.2. Segregation to the Σ3 coherent annealing twin boundary (GB2)

In general, coherent twin boundaries are known for their low interfacial free energies and low free volume [59–61]. Therefore, it has been commonly assumed that solute segregation does not occur at these types of GBs [62]. However, recent HRTEM experiments in α-Mg proved that even ideally coherent twin boundaries can be subject to solute segregation [62]. Moreover, slight deviations from the ideal Σ3 orientation relation or from the coherent GB plane orientation is accommodated by misfit dislocations and interface facets, respectively, which give rise to GB segregation that scales with the density of such defects at the boundary [36]. It is thus of great importance to determine the macroscopic crystallographic GB parameters as accurately as possible when investigating segregation. The misorientation of GB2 was determined by EBSD using standard parameters that are reported to yield an angular resolution of about 1° [63]. However, this is valid for the individual measurement point and can be improved by calculating the average orientation based on several measurement points, provided that the grains contain no intragranular orientation gradient. The latter is assumed to be the case in the current work as the material was

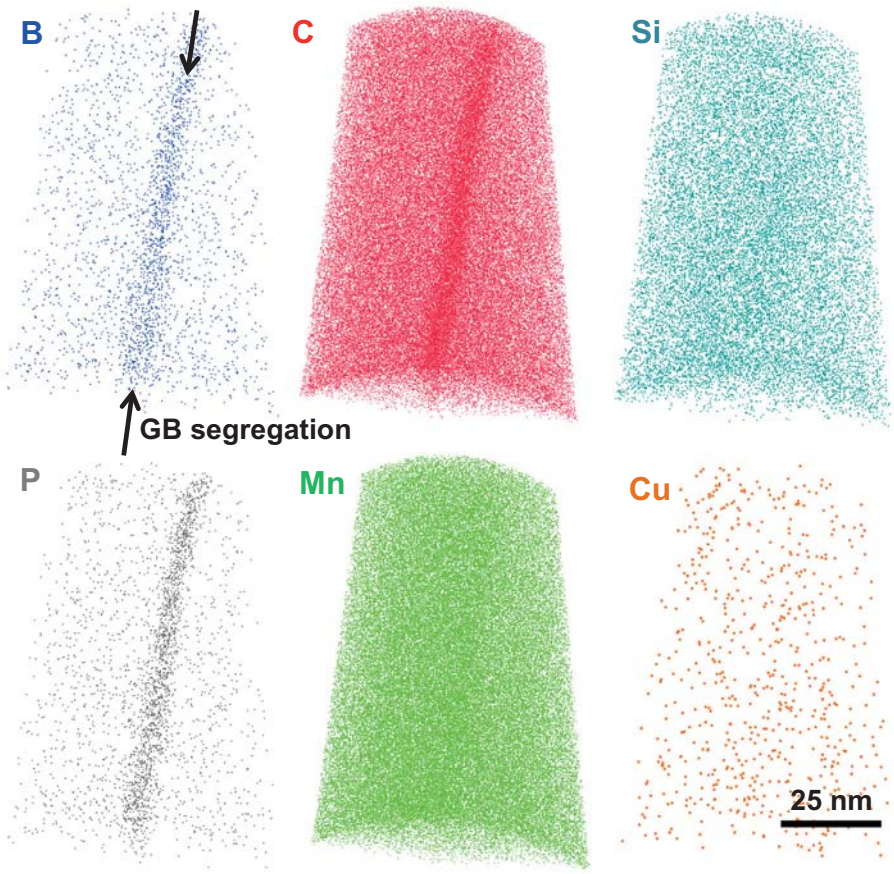

Fig. 5. 3-D elemental atom maps (12 million atoms total) containing GB1, viewed edge-on.

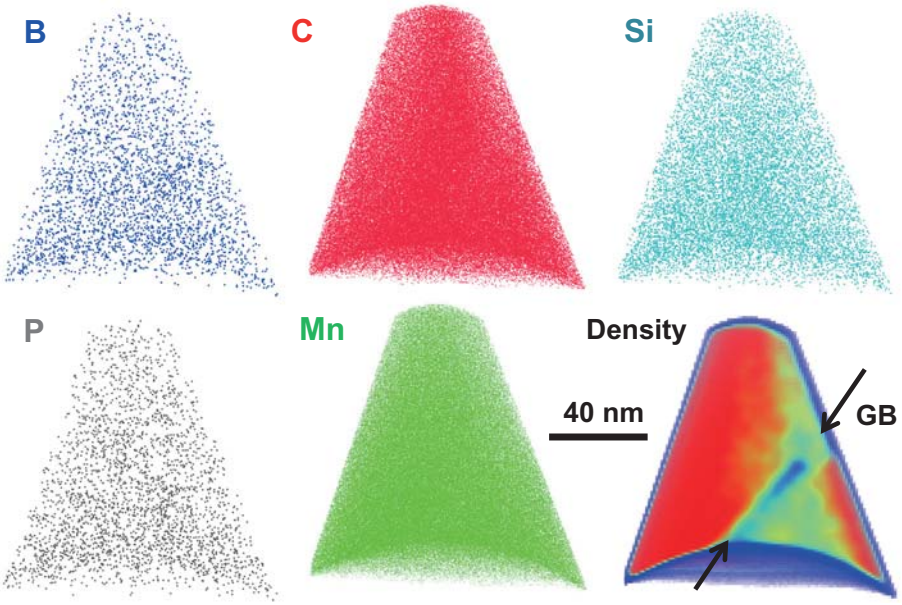

Fig. 6. 3-D elemental atom maps (16 million atoms total) containing GB2, viewed edge-on. A planar region of decreased iron density (bottom right map) identifies the position of the grain boundary.

recrystallized, and was also confirmed by a grain reference orientation deviation analysis on the EBSD dataset. Based on an average grain orientation calculated from at least 1500 measurement points for each of the abutting grains, the deviation from the ideal Σ3 orientation relationship of GB2 amounts to only 0.17°. The corresponding standard deviations of the average grain orientations for the two grains of GB2 were 0.19 and 0.43°. However, the EBSD

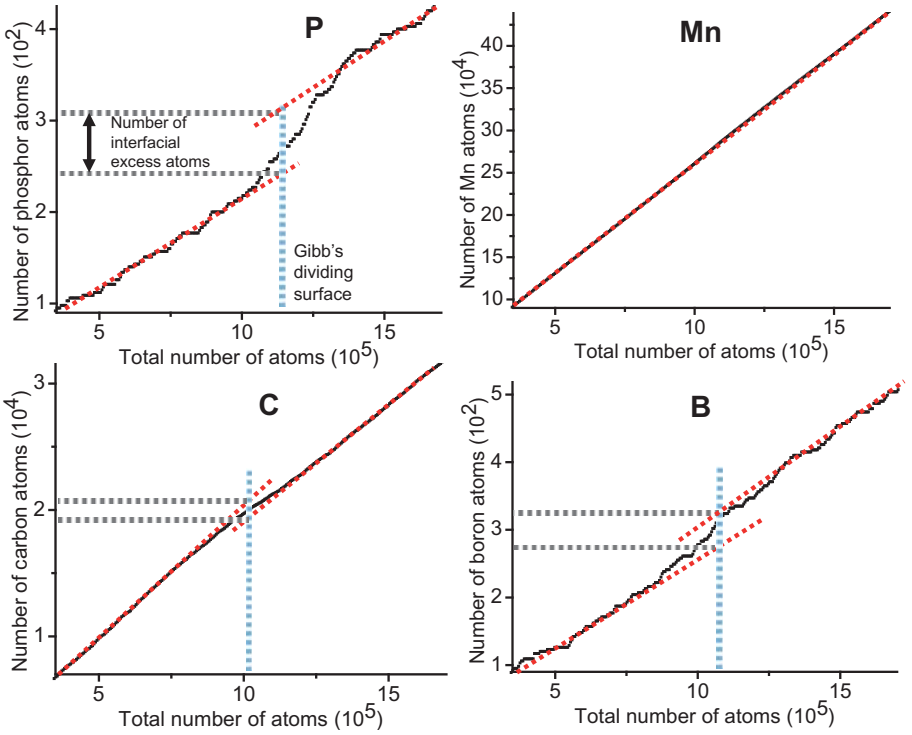

Fig. 7. Ladder diagrams determined from a cylindrical region of interest with 27 nm diameter, perpendicular to GB2.

Table 2. Grain boundary excess values (in atoms nm^{-2}), quantified from ladder diagram plots such as those in Fig. 7.

Grain boundary	B	C	Si	P	Mn	Cu
General GB (GB1, 52°[675])	0.53 ± 0.01	6.6 ± 0.5	0.16 ± 0.04	0.62 ± 0.02	–	0.03 ± 0.01
Σ3 coherent twin (GB2, 60°[1 1 1])	0.10 ± 0.03	-2.7 ± 0.8	0.26 ± 0.06	0.10 ± 0.02	–	–

orientation analysis still has a certain error associated with it and also the SEM measurement of the GB plane inclination, as shown in Fig. 4. Therefore, the absolute coherency of GB2 investigated here cannot be definitively proved. Nevertheless, a number of facts suggest that GB2 is an ideal coherent twin boundary: (i) the twin was created in the course of recrystallization during an extended heat treatment (24 h at 700 °C) so that relaxation to full coherency is likely; (ii) the EBSD orientation analysis fits almost perfectly to the ideal misorientation relationship; (iii) the samples were not mechanically loaded; (iv) the GB plane continuation in depth, as measured by SEM in the cross-sections of the lift-out sample, fits almost perfectly to the {1 1 1} plane; and (v) segregation at the GB is so subtle that it was not detectable by conventional means using the IVAS software.

Tomozawa et al. [39] conducted an APT analysis of a Σ3 boundary in 316L stainless steel that was solution-treated at 1043 °C for 15 h and water quenched. Although the authors did not specify the GB plane, based on the fact that no segregation was found, it can be assumed that the boundary was also a coherent twin boundary like those in the case investigated here. One possible explanation for why the authors detected no segregation is that they performed annealing at a higher temperature, which decreases the solute segregation according to the Gibbs adsorption isotherm [34]. The other possible reason is that only a visual inspection of the density of atoms was performed. As demonstrated in the current work, this method is not suitable for accurate quantification of whether solute segregation or depletion occurs at a coherent Σ3 annealing twin boundary.

The APT analysis of the coherent Σ3 annealing twin boundary (GB2) in the current work shows that Gibbs excess values for B and P are drastically reduced as compared to the general GB (GB1). This can be explained by the fact that the highly symmetric GB2 is a low-energy GB [31] and thus requires correspondingly less solute segregation to be rendered stable [64,65]. The element Cu follows the same trend as B and P for the same reason. However, as it is on the verge of the detection limit in the case of GB1, it is below that limit in the case of GB2.

Only the element C behaves unexpectedly. Detection of less pronounced segregation of C at GB2 compared to GB1 might have been expected, but instead a considerable negative value of the Gibbs excess was measured (Table 2). This is in fact consistent with recent results of Hickel et al. [66], who investigated the segregation of C to stacking faults in fcc iron in Fe–22Mn–0.6C (wt.%), which is a very similar alloy to the one probed here. The ab initio simulations revealed that the change in the fcc stacking sequence from ABCABC to ABAB at the stacking fault generates a hexagonal close-packed (hcp) crystal structure locally, which constitutes an energetically unfavorable environment for C. Given enough energy to overcome a significant activation energy barrier – in Ref. [66] by a 200 kV electron beam in the transmission electron microscope at room temperature – a thin carbon-depleted area forms at the stacking fault

(the so called "anti-Suzuki effect" [67]), which lowers the stacking fault energy locally and thus causes an increase in the partial dislocation separation distance [66]. Since a Σ3 coherent twin in fcc consists of stacking faults on consecutive {1 1 1} planes [68] and thus also creates a local hexagonal ABAB stacking sequence, the same mechanism as in Ref. [66] applies in the scenario observed here. The high temperature (700 °C) during annealing provides enough energy for C to leave the local hcp phase and this explains the depletion of C at GB2.

4.3. Segregation to deformation twin boundaries

Deformation twins and annealing twins are crystallographically identical in terms of their five geometric degrees of freedom [68], although additional partial dislocations or ledges along deformation twins can exist [69]. The main difference is the way in which they are formed, namely, the annealing twin by diffusion at elevated temperature [68] and the deformation twin through a mechanical shear mechanism [16], usually at lower temperature. Since equilibrium solute segregation at the twin boundary, as well as solute diffusion, are temperature-dependent quantities, it is likely that these interfaces (annealing twin vs. deformation twin) contain different local chemical compositions. As such, previously published APT data [70] containing a high density of deformation twins have been reinvestigated using the same analysis routine as for the annealing twin boundary GB2. In Ref. [70] the specimens of an Fe–22Mn–0.6C (wt.%) alloy with a similar composition to that of the current work were subjected to 30% tensile deformation at room temperature and no solute segregation to the deformation twin boundaries was detected by conventional APT analysis.

Fig. 8a shows a bright-field scanning transmission electron microscopy (STEM) image of an atom probe tip containing several nanoscale deformation twins. Although the difference in contrast is faint due to their superposition with a low-density pole region that passes straight through the volume, Fig. 8b reveals the deformation twins, which appear as a stairway pattern on both sides of the pole. The comparison between Fig. 8a and b shows that the number, orientation and spacing between the twins and the stairway patterns are in good agreement. Fig. 8c shows an APT volume of an undeformed Fe–28Mn–0.3C (wt.%) sample that contained no twins, visualized using the same parameters as for Fig. 8b. This data also contains a low-density crystallographic pole; however, no stairway pattern is visible. The stairway pattern observed in Fig. 8b is therefore very likely to be caused by the deformation twins, and represents their position in the dataset. However, when the same ladder-diagram analysis was applied to the deformation twins, as described earlier for both GB1 and GB2, no chemical variations (segregation or depletion) were detected.

These experimental results demonstrate a significant difference in the local chemistry between annealing twin and deformation twin interfaces. For the elements B and P, this is not surprising, given their low diffusion coefficients at room temperature of 5.6×10^{-40} and 6.9×10^{-23} $cm^2\,s^{-1}$, respectively (calculated using Thermo-Calc software, Mob2 database), and given the sparse, homogeneous distribution in the matrix due to the low alloy concentration (see Table 1), which means that the atoms would have to migrate long distances to enrich at the GB. An absence of C depletion at the deformation twin interfaces is more surprising. This element also has a low diffusion coefficient in austenite at room temperature, of 2.5×10^{-31} $cm^2\,s^{-1}$, but diffusion of only a few atomic distances would be required to leaving the local hcp zone (stacking fault). Hickel et al. [66] described C depletion at stacking faults as occurring due to the energy input from a 200 kV electron

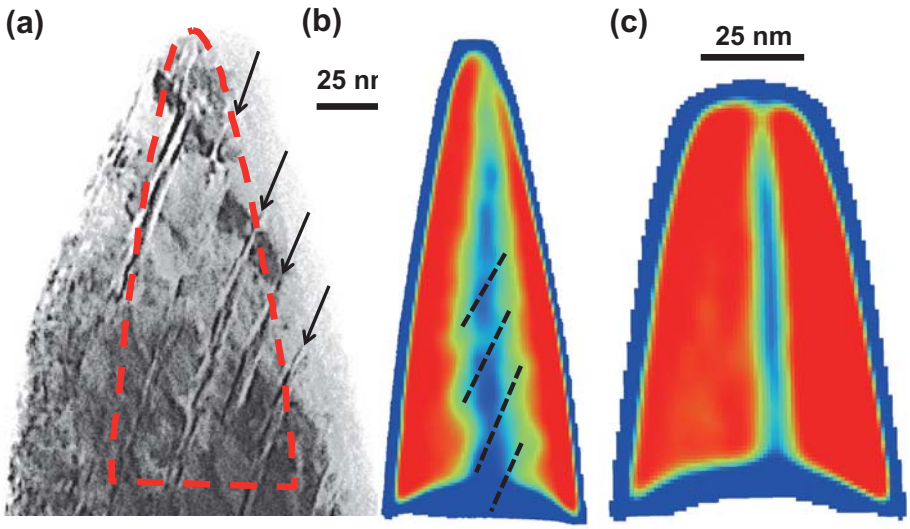

Fig. 8. Correlative STEM (a) and APT (b) investigation of deformation twins in Fe–22Mn–0.6C (wt.%) deformed to 30% strain at room temperature. The visibility of the nanotwins (indicated by black arrows) was increased in the STEM micrograph by an image-sharpening algorithm. The red dashed line indicates the position of the atom probe dataset depicted in (b), which shows a color-coded volume rendering of the density distribution in the sample. Delocalization parameters of 6 nm × 6 nm × 10 nm were applied in the IVAS software and blue and red represent low and high density regions, respectively. The blue column in the center indicates the presence of a crystallographic pole. The stairway pattern on both sides along the pole indicates the superposition of the nanotwins (black dashed lines), which also have a lower density than the bulk. (c) Reference APT density map of an undeformed Fe–28Mn–0.3C (wt.%) sample containing only a single grain without deformation twins and also showing a crystallographic pole. The same visualization parameters were applied in (b) and (c). (For interpretation of the references to colour in this figure legend, the reader is referred to the web version of this article.)

beam – the same as that used for the correlative STEM images taken in the case of the deformation twins [70]. This discrepancy could be explained by the fact that the TEM experiments carried out by Hickel et al. provided greater energy for C diffusion as they worked with a LaB_6 thermionic electron source, whereas less energy was input during the STEM measurements in Ref. [70] since these were performed using a field-emission gun that had a two orders of magnitude lower primary beam current compared to thermionic electron sources [71,72]. Additionally, in the case of Ref. [70], the sample exposure to the electron beam was kept as short as possible so as not to cause C contamination on the surface of the APT tip sample, as this can cause early failure of the tip in the atom probe experiment. It can be concluded, therefore, that the activation energy barrier for diffusion of C out of the local hcp structure at the deformation twin is so high that a rather intense electron beam, or temperatures clearly above room temperature, are needed to cause the formation of a C-depleted zone at a deformation twin. Thus, the difference in local chemical composition (i.e. the solute segregated or depleted nature at the interface) between annealing and deformation twin boundaries is most likely due to their different formation temperatures. It can therefore be expected that, despite their crystallographic identity, these boundary-type variants differ in GB energy, possess different resistance to the transmission of dislocations and impart different material properties, e.g. different corrosion and embrittlement behavior.

Atomistic simulations [73] show that twin boundaries are not insuperable obstacles for dislocations, as is normally the case for general GBs, and this accounts for the fact that TWIP materials display high ductility. During deformation, however, dislocations can interact with the twin boundaries, resulting in sessile dislocations, stacking faults and steps along the boundary, all of which cause a loss of coherency. The capacity of twin boundaries to accumulate these lattice defects in high densities explains the exceptional work-hardening behavior of these materials [74]. Lattice defects at twin boundaries will attract solute atoms if provided with enough activation energy for segregation by diffusion. Deformed TWIP steels that were exposed to elevated temperatures could thus show much higher levels of segregation at deformation or annealing twins than measured at the annealing twin in this work. These concepts provide a framework for GB engineering by solute segregation [75,76] of high-Mn TWIP steels using appropriate thermomechanical processing to control both volume fraction of, and segregation to, certain boundary types and, thereby, influence the mechanical and functional properties.

4.4. Influence of segregation on the nucleation of deformation twins

The critical stress for the formation of deformation twins is directly related to the SFE [3], which is a function of the chemical composition [17,18]. According to Mahajan's model, deformation twins nucleate at GBs [16] and thus local chemical changes due to GB segregation should also affect the twin nucleation behavior. For the two investigated boundaries, GB1 and GB2, the element C is quantitatively by far the most important segregated element. The enrichment of C at the general GB (GB1) causes an increase in the local SFE [17] and thus an increase in the critical stress for twin formation. Correspondingly, twin formation at the boundary of this (general) type should be more difficult. The depletion of C at the deformation twin (GB2) should cause the opposite and facilitate twin nucleation or formation of epsilon martensite, depending on the exact local SFE.

Our results indirectly confirm Hickel et al.'s [66] assumption that the nanodiffusion of C away from a stacking fault is responsible for a local change in the SFE. The results also indicate that these processes do not happen at room temperature, thus their influence on the mechanical deformation at room temperature is not expected. However, at elevated temperatures, where the C depletion at stacking faults causes a reduction in the stacking fault energy and thus a reduction in the critical stress for twin formation, an impact on the mechanical properties could be distinct.

4.5. Embrittlement as consequence of GB segregation

In body-centered cubic (bcc) iron-based alloys, Mn is reported to segregate to interfaces, where it can cause embrittlement even after short annealing times at 450 °C [77]. Huang et al. [20] observed an increased tendency for intergranular fracture of austenitic Fe–Mn–C TWIP steels with increasing Mn content, which they explained by higher amounts of Mn GB segregation in these alloys. However, in fcc iron alloys Mn seems not to segregate to the interfaces. Neither Tomozawa et al. [39], who investigated GB segregation in 1.5 wt.% Mn steel by APT and reported Mn enrichment at the GB, nor our measurements of the local chemical composition at the GBs support the assumption of Huang et al. As reported and discussed above, for all of the GBs investigated here, Mn was neither enriched nor depleted at the interface. Also, if recrystallization were to be performed at 950 °C, like in the case of Huang et al. to wit at a temperature 250 °C higher than in the case investigated here, enrichment of Mn at the GB would not be expected, as the Gibbs adsorption isotherm predicts even lower amounts of equilibrium segregation at higher temperatures [34]. What is responsible for the increased tendency for intergranular fracture with increased Mn content as reported by Huang et al. is thus unknown, but there is strong evidence that it is not related to Mn GB segregation.

The embrittlement effect of P in bcc iron has been known for a long time [78]. According to first-principles studies by Yuasa and Mabuchi [79], P at a $\Sigma3(1\,1\,1)/[1\text{-}1\,0]$ GB in bcc iron has an embrittling effect as the element causes covalent-like bonding characteristics. However, there are no reports on GB embrittlement in austenitic alloys, although P also segregates to the interfaces [58]. The measured P GB segregation in the Fe–Mn–C TWIP steels thus seems not to be harmful to the mechanical properties of this type of alloy, owing to their austenitic crystal structure.

Fe–Mn–C TWIP steels have not been reported to show pronounced intergranular fracture in the absence of H. In the current work, we measured significant compositional differences between general GBs, and annealing twin and deformation twin boundaries. If the presence of any of the segregated elements played a role in H embrittlement, e.g. by attracting higher amounts of H or by forming brittle H complexes, one would expect certain boundary types to be more prone to H embrittlement than others. However,

Koyama et al. [29] reported hydrogen-assisted cracking at all boundary types, including Σ3 coherent annealing twins and deformation twins. This indicates that H itself has embrittling properties and that the presence of other elements at the GB plays a subordinate role. Recent ab initio calculations [31,32][1] indicate that GBs with an "open" structure (such as a general GB) offer many attractive binding sites for H, whereas GBs with a "closed" structure (such as Σ3 coherent twins) in fcc do not attract H. Hydrogen equilibrium segregation to GBs could thus explain the hydrogen embrittlement of general GBs but not of annealing or deformation twins. This suggests that H-assisted fracture of annealing and deformation twins might be related more to H interaction with the tip of a crack that initiated elsewhere (e.g. at triple points) than with H equilibrium GB segregation.

5. Summary and conclusions

Grain boundary segregation in an Fe–Mn–C TWIP steel was investigated by APT in three representative cases: in specimens with a general GB, an annealing twin boundary and a deformation twin boundary. All boundaries were found to differ significantly in their local chemical composition. The general GB exhibited segregation of B, C, Si and P, and traces of Cu. The annealing twin also displayed segregation of B and P but at much lower Gibbs excess values than the general GB. Additionally, and in contrast to the general GB, depletion of C was found at the annealing twin boundary. This is explained by a change in the stacking sequence, which creates a local hcp structure with low C solubility. Although the deformation twin boundary is crystallographically identical to the annealing twin boundary, no evidence for segregation at the deformation twin boundary was found. This is attributed to the lack of diffusivity of the solutes at room temperature. Apparently, the different chemical composition of annealing twins and deformation twin boundaries is a general phenomenon, owing to their different temperatures of formation. Neither Mn enrichment nor depletion was detected at any GBs. It is expected that the enrichment of C at general GBs causes an increase in the local SFE and thus an increase in the critical stress for twin formation. On the other hand, the depletion of C at annealing twin boundaries should cause the opposite effect and serve to facilitate twin nucleation. The overall effect of GB segregation on mechanical properties remains to be investigated, given a certain balance or volume fraction of these boundary segregation/depletion scenarios within a high-Mn TWIP steel system at various stages of tensile strain deformation and at various strain rates. During deformation at elevated temperatures, where the diffusivity of C is high enough for its depletion at twin boundaries, the local reduction in the SFE could have an impact on the mechanical properties. Despite their crystallographic identity, annealing and deformation twin boundaries may differ, due to their different segregation chemistries, in (i) corrosion and embrittlement behavior; (ii) GB energy; and (iii) resistance against the transmission of dislocations.

[1] Du et al. and Hickel et al. describe calculations of 70.5°[1-10]{111} twins. These are crystallographically identical to the 60°[111]{111} annealing and deformation twins described in this work.

Acknowledgements

The authors acknowledge financial support by the German Research Foundation (DFG) through funding of the SFB 761 "steel ab initio" project. R.K.W.M. acknowledges the support of the Alexander von Humboldt Foundation through the award of a Humboldt Postdoctoral Fellowship. M.K. gratefully acknowledges the ERC Advanced Grant "Smartmet" for funding. The authors further acknowledge Stefan Zaefferer for support with the EBSD analysis.

References

[1] C. Scott, S. Allain, M. Faral, N. Guelton, Rev. Metall. Paris 103 (2006) 293.
[2] O. Bouaziz, S. Allain, C.P. Scott, P. Cugy, D. Barbier, Curr. Opin. Solid State Mater. 15 (2011) 141.
[3] D.R. Steinmetz, T. Japel, B. Wietbrock, P. Eisenlohr, I. Gutierrez-Urrutia, A. Saeed-Akbari, et al., Acta Mater. 61 (2013) 494.
[4] I. Gutierrez-Urrutia, D. Raabe, Acta Mater. 59 (2011) 6449.
[5] I. Gutierrez-Urrutia, D. Raabe, Acta Mater. 60 (2012) 5791.
[6] I. Gutierrez-Urrutia, S. Zaefferer, D. Raabe, Mater. Sci. Eng. A Struct. 527 (2010) 3552.
[7] G. Frommeyer, U. Brux, P. Neumann, ISIJ Int. 43 (2003) 438.
[8] O. Grassel, L. Kruger, G. Frommeyer, L.W. Meyer, Int. J. Plast. 16 (2000) 1391.
[9] C. Haase, L. Barrales-Mora, F. Roters, D. Molodov, G. Gottstein, Acta Mater. 80 (2014) 327.
[10] C. Haase, S.G. Chowdhury, L.A. Barrales-Mora, D.A. Molodov, G. Gottstein, Metall. Mater. Trans. A 44A (2013) 911.
[11] Y.P. Lu, D.A. Molodov, G. Gottstein, Acta Mater. 59 (2011) 3229.
[12] Y.P. Lu, D.A. Molodov, G. Gottstein, ISIJ Int. 51 (2011) 812.
[13] J.W. Cahn, Acta Metall. Mater. 10 (1962) 789.
[14] K. Lucke, H.P. Stuwe, Acta Metall. Mater. 19 (1971) 1087.
[15] S. Mahajan, Philos. Mag. 23 (1971) 781.
[16] S. Mahajan, G.Y. Chin, Acta Metall. Mater. 21 (1973) 1353.
[17] A. Saeed-Akbari, L. Mosecker, A. Schwedt, W. Bleck, Metall. Mater. Trans. A 43A (2012) 1688.
[18] A. Saeed-Akbari, J. Imlau, U. Prahl, W. Bleck, Metall. Mater. Trans. A 40A (2009) 3076.
[19] M. Koyama, T. Sawaguchi, K. Tsuzaki, Metall. Mater. Trans. A 43A (2012) 4063.
[20] Y. Huang, A.M. Zhao, Z.L. Mi, H.T. Jing, W.Y. Li, Y.J. Hui, J. Iron Steel Res. Int. 20 (2013) 111.
[21] R.K.S. Raman, M. Khalissi, S. Khoddam, Metall. Mater. Trans. A 45A (2014) 1979.
[22] S. Hong, S.Y. Shin, H.S. Kim, S. Lee, S.K. Kim, K.G. Chin, et al., Metall. Mater. Trans. A 44A (2013) 776.
[23] H.C. Lin, K.M. Lin, C.S. Lin, T.M. Ouyang, Corros. Sci. 44 (2002) 2013.
[24] M.J. Duarte, J. Klemm, S.O. Klemm, K.J.J. Mayrhofer, M. Stratmann, S. Borodin, et al., Science 341 (2013) 372.
[25] K.G. Chin, C.Y. Kang, S.Y. Shin, S. Hong, S. Lee, H.S. Kim, et al., Mater. Sci. Eng. A Struct. 528 (2011) 2922.
[26] Y.S. Chun, K.T. Park, C.S. Lee, Scr. Mater. 66 (2012) 960.
[27] M. Koyama, E. Akiyama, T. Sawaguchi, D. Raabe, K. Tsuzaki, Scr. Mater. 66 (2012) 459.
[28] M. Koyama, E. Akiyama, K. Tsuzaki, Corros. Sci. 59 (2012) 277.
[29] M. Koyama, E. Akiyama, K. Tsuzaki, D. Raabe, Acta Mater. 61 (2013) 4607.
[30] M. Koyama, E. Akiyama, K. Tsuzaki, Corros. Sci. 54 (2012) 1.
[31] Y.J.A. Du, L. Ismer, J. Rogal, T. Hickel, J. Neugebauer, R. Drautz, Phys. Rev. B (2011) 84.
[32] T. Hickel, R. Nazarov, E. McEniry, G. Leyson, B. Grabowski, J. Neugebauer, J. Met. 66 (8) (2014) 1399.

[33] B.L. He, W. Xiao, W. Hao, Z.X. Tian, J. Nucl. Mater. 441 (2013) 301.
[34] J.W. Gibbs, The Collected Works of J. Willard Gibbs, Yale University Press,, New Haven, CT, 1948.
[35] P. Lejcek, Grain Boundary Segregation in Metals, Springer Verlag, Berlin, 2010.
[36] M. Herbig, D. Raabe, Y.J. Li, P. Choi, S. Zaefferer, S. Goto, Phys. Rev. Lett. (2014) 112.
[37] S.I. Baik, M.J. Olszta, S.M. Bruemmer, D.N. Seidman, Scr. Mater. 66 (2012) 809.
[38] P. Felfer, S.P. Ringer, J.M. Cairney, Ultramicroscopy 111 (2011) 435.
[39] M. Tomozawa, Y. Miyahara, K. Kako, Mater. Sci. Eng. A Struct. 578 (2013) 167.
[40] L. Yao, S.P. Ringer, J.M. Cairney, M.K. Miller, Scr. Mater. 69 (2013) 622.
[41] S. Mandal, K.G. Pradeep, S. Zaefferer, D. Raabe, Scr. Mater. 81 (2014) 16.
[42] R. Jones, V. Randle, Mater. Sci. Eng. A Struct. 527 (2010) 4275.
[43] V. Randle, Mater. Sci. Technol. Lond. 26 (2010) 774.
[44] K. Thompson, D. Lawrence, D.J. Larson, J.D. Olson, T.F. Kelly, B. Gorman, Ultramicroscopy 107 (2007) 131.
[45] D.G. Brandon, Acta Metall. Mater. 14 (1966) 1479.
[46] V. Randle, Microtexture Determination and its Applications, Institute of Materials, Minerals and Mining, London, 2013.
[47] V. Randle, Scr. Mater. 44 (2001) 2789.
[48] R.K.W. Marceau, P. Choi, D. Raabe, Ultramicroscopy 132 (2013) 239.
[49] B.W. Krakauer, D.N. Seidman, Phys. Rev. B 48 (1993) 6724.
[50] D.N. Seidman, B.W. Krakauer, D. Udler, J. Phys. Chem. Solids 55 (1994) 1035.
[51] S. Zaefferer, Adv. Imag. Electron Phys. 125 (2002) 355.
[52] S. Zaefferer, J. Appl. Crystallogr. 33 (2000) 10.
[53] L. Liu, J. Wang, S.K. Gong, S.X. Mao, Sci. Rep. UK (2014) 4.
[54] P.J. Felfer, B. Gault, G. Sha, L. Stephenson, S.P. Ringer, J.M. Cairney, Microsc. Microanal. 18 (2012) 359.
[55] B. Gault, M. Moody, J.M. Cairney, S.P. Ringer, Atom Probe Microscopy, Springer, Berlin, 2012.
[56] P. Lejcek, S. Hofmann, Crit. Rev. Solid State 20 (1995) 1.
[57] C.L. Briant, P.L. Andresen, Metall. Trans. A 19 (1988) 495.
[58] M. Paju, H.J. Grabke, Mater. Sci. Technol. Lond. 5 (1989) 148.
[59] R.L. Fullman, J. Appl. Phys. 22 (1951) 448.
[60] G.S. Rohrer, J. Mater. Sci. 46 (2011) 5881.
[61] J. Wang, N. Li, A. Misra, Philos. Mag. 93 (2013) 315.
[62] J.F. Nie, Y.M. Zhu, J.Z. Liu, X.Y. Fang, Science 340 (2013) 957.
[63] S. Zaefferer, Cryst. Res. Technol. 46 (2011) 607.
[64] R. Kirchheim, Acta Mater. 50 (2002) 413.
[65] M.P. Seah, E.D. Hondros, Proc. R. Soc. Lond. Ser. A Math. Phys. Eng. Sci. 335 (1973) 191.
[66] T. Hickel, S. Sandloebes, R.K.W. Marceau, A. Dick, I. Bleskov, J. Neugebauer, et al., Acta Mater. 75 (2014) 147.
[67] H. Suzuki, J. Phys. Soc. Jpn. 17 (1962) 322.
[68] S. Mahajan, C.S. Pande, M.A. Imam, B.B. Rath, Acta Mater. 45 (1997) 2633.
[69] K. Lu, L. Lu, S. Suresh, Science 324 (2009) 349.
[70] R.K. Marceau, I. Gutierrez-Urrutia, M. Herbig, K.L. Moore, S. Lozano-Perez, D. Raabe, Microsc. Microanal. (2013) 1.
[71] D.B. Williams, C.B. Carter, Transmission Electron Microscopy, Part 1: Basics, Springer Science + Business Media, New York, 2009.
[72] L. Hobbs, Introduction to Analytical Electron Microscopy, Plenum Press, New York, 1979.
[73] T. Zhu, J. Li, A. Samanta, H.G. Kim, S. Suresh, Proc. Natl. Acad. Sci. USA 104 (2007) 3031.
[74] M. Dao, L. Lu, Y.F. Shen, S. Suresh, Acta Mater. 54 (2006) 5421.
[75] D. Raabe, M. Herbig, S. Sandlöbes, Y.J. Li, D. Tytko, M. Kuzmina, et al., Curr. Opin. Solid State Mater. Sci. 18 (2014) 253.
[76] D. Raabe, S. Sandlobes, J. Millan, D. Ponge, H. Assadi, M. Herbig, et al., Acta Mater. 61 (2013) 6132.
[77] F. Nikbakht, M. Nasim, C. Davies, E.A. Wilson, H. Adrian, Mater. Sci. Technol. Lond. 26 (2010) 552.
[78] W.A. Spitzig, Metall. Trans. 3 (1972) 1183.
[79] M. Yuasa, M. Mabuchi, Mater. Trans. 52 (2011) 1369.